Research Article | Vol. 33, No. 5 / 10 Mar 2025 / Optics Express 10726
Optics EXPRESS

Reconfigurable electrostatically actuated 1 × 5 rotary MOEMS switch

NAVID HEIDARI,* JULIAN L. PITA RUIZ, SEYEDFAKHREDDIN NABAVI, MICHAËL MÉNARD, AND FREDERIC NABKI

Department of Electrical Engineering, École de Technologie Supérieure, Montréal, QC, H3C 1K3, Canada
navid.heidari.1@ens.etsmtl.ca

Abstract: Optical switches play a critical role in optical communication systems, meeting the growing demand for high-speed data transfer. Among optical switches, micro-opto-electro-mechanical system (MOEMS) switches stand out for their reconfigurability and broadband capability, making them well-suited for applications in data centers. In this article, we present, to our knowledge, a novel 1×5 rotary MOEMS switch actuated by an electrostatic comb-drive for optical networking. The rotary in-plane platform is integrated with silicon nitride (SiN) waveguides, enabling the switch to operate across a broad spectral range in both polarizations. Experimental results demonstrate that the switch platform achieves a rotation of 2.6° in the counterclockwise direction and 2.9° in the clockwise direction, covering five waveguides, with a measured average power loss of −5.57 dB across all channels over the spectrum of 1540 nm to 1625 nm.

1. Introduction

The growing need for digital communications and the increasing use of bandwidth-intensive applications, such as video streaming, have led to an exponential increase in the demand for efficient network management and high-speed data transmission. High-speed interconnects are critical in data centers. Due to their high power dissipation, electrical interconnects, which are usually copper-based, present significant obstacles to increasing data transmission rates [1]. The limitations of electrical interconnects may be addressed by optical interconnects and photonic integrated circuits (PICs), which have the potential to achieve high data transmission speeds [2] and low power consumption [3,4]. For instance, fully optical terabit-per-second communications links in data centers were demonstrated by Bernabe *et al.* [5].

Optical switches are used in data centers to dynamically manage and route data traffic, providing high capacity and efficient connectivity. These switches enable the reconfiguration of network pathways to handle varying traffic loads without manual intervention, enhancing the performance and efficiency of data centers. They provide low-latency connections, minimize power loss, and reduce crosstalk, which is crucial for maintaining high-speed data transmission [6].

Different types of optical switches were demonstrated for use in data center networks [7,8], including multi-mode interference (MMI) [9,10] and Mach-Zehnder interferometer (MZI) switches [11–14], and MOEMS switches [15,16]. Compared to conventional MMI and MZI switches, MOEMS switches have benefits, such as a wide bandwidth [17]. Moreover, while MMI and MZI switches employ interference effects to manipulate signals, MOEMS switches can achieve reconfigurability by physically rearranging their optical channels. MOEMS switches also typically show higher extinction ratios and reduced crosstalk [18]. Most of the MOEMS switches that have been demonstrated were integrated with silicon photonics. However, combining silicon waveguides with MEMS on the device layer of silicon-on-insulator (SOI) wafers leads to device trade-offs, as the layer of material in SOI used for the MEMS structure is the same for optical waveguides. Modifying the thickness of this layer affects the optical and mechanical properties of the switch [19].

#545403 https://doi.org/10.1364/OE.545403
Journal © 2025 Received 23 Oct 2024; revised 18 Dec 2024; accepted 8 Jan 2025; published 3 Mar 2025

Optics EXPRESS

Recently, silicon nitride (SiN) has attracted interest to implement optical switches due to its high thermal stability, lower fabrication sensitivity, and lower refractive index [20,21]. Moreover, since SiN has a lower refractive index than silicon, this reduces mode confinement, which helps minimize optical losses and improve the overall efficiency of the waveguide. This makes SiN a promising candidate for integrated photonics, especially since it is transparent over a wide range of wavelengths. A few optical switches have utilized SiN, such as the MZI switch presented by L. Dong *et al.* [22], and MOEMS switches presented in [17,23–26]. For instance in [23], the 1×3 MOEMS switch has a minimum and maximum insertion loss of 4.64 dB and 5.83 dB, respectively, in different switching positions. In the electrothermally actuated MOEMS positioner presented in [26], the insertion loss is 1.6 dB. Both of these MOEMS switches demonstrate how MEMS can take advantage of the broadband performance of SiN waveguides. However, aligning SiN waveguides is challenging due to the residual stress of the oxide on the structure, which is one of the trade-offs of using SiN waveguides.

In this work, we present an electrostatically actuated rotary MOEMS switch integrated with SiN waveguides that is inspired by [27]. However, we designed a new configuration for the actuators and an improved spring system including circular-shaped springs. It results in increment of the number of waveguides in the switch and enhanced the rotational mechanism of the MEMS structure. The utilization of electrostatic actuation results in near-zero power consumption. Integrating the MEMS structure with 850 nm × 435 nm SiN waveguides enables the rotary MOEMS switch to operate in a single-mode condition across a broad spectral range. The rotary MEMS switch accommodates 7 optical waveguides, with a displacement of 2.9° clockwise (CW) and 2.6° counterclockwise (CCW), thereby covering 5 channels out of the 7 available within the structure. The average optical power loss measured is −5.57 dB across the measured spectrum range from 1540 nm to 1625 nm.

2. Design

The proposed optical rotary switch is comprised of a silicon MEMS structure onto which SiN optical waveguides are integrated. Figure 1(a) shows a top view of the rotary switch schematic. The following details the operating principle and device structure.

2.1. Operating principle

The MOEMS switch comprises a single input waveguide and seven output waveguides, aligned with the electrode labeled V_{GC} and positioned on a suspended platform, supported by serpentine springs, as depicted in Fig. 1(b). The complete suspended structure is shown in Fig. 1(c), highlighting the circular springs that enable rotational movement. The waveguides incorporate surface grating couplers to facilitate light transmission into and out of the chip. The input waveguide extends along the length of the electrode to the suspended platform, where a necessary gap is present to accommodate the rotation of the platform. This gap introduces a discontinuity between the waveguides on the platform and the output waveguides, as illustrated in Fig. 1(d).

Light enters the input waveguide and is directed to one of the waveguides on the platform. To achieve this, the platform rotates to align the desired waveguide with the input waveguide. The rotation of the platform is actuated by comb drives located on both sides, allowing for rotation in both CW and CCW directions, as shown in Fig. 1(a). Once the waveguide on the platform is aligned with the input waveguide, the light propagates through the aligned waveguide on the platform and exits via the corresponding output waveguide.

Initially, when the input waveguide is aligned with any of the waveguides on the suspended platform and the output waveguides, significant power loss occurs due to the two gaps between the input waveguide, the waveguide on the platform, and the output waveguide. To reduce this insertion loss, it is crucial to close the gaps between these waveguides. This can be achieved

Optics EXPRESS

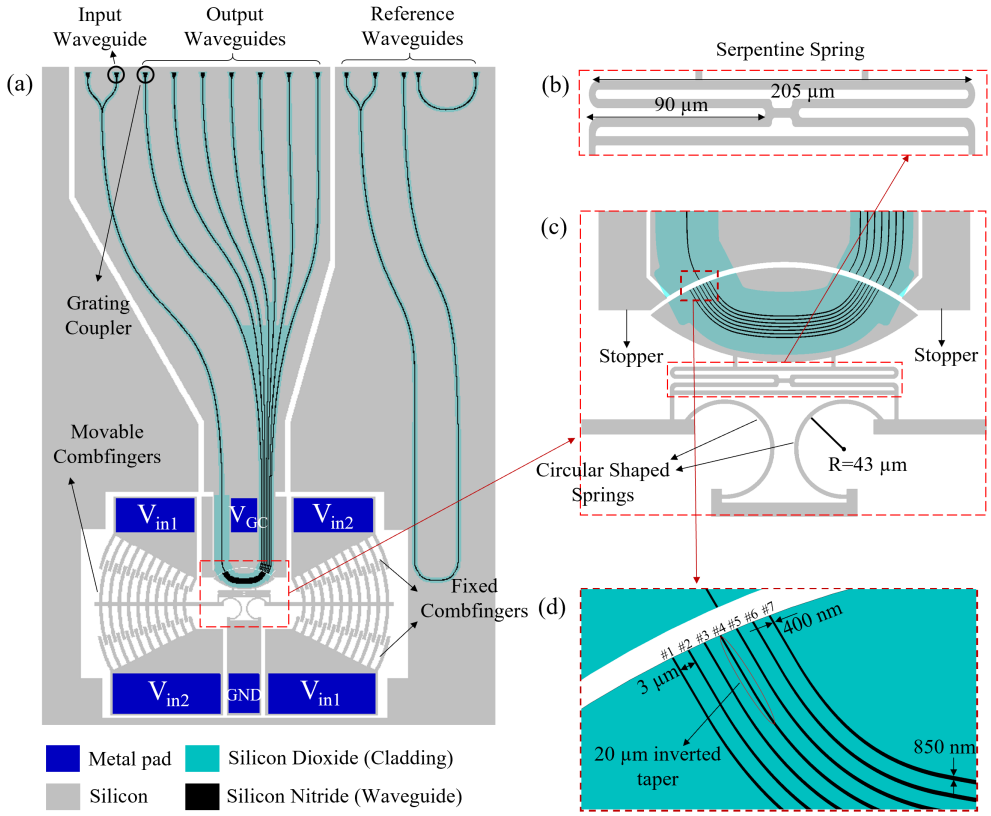

Fig. 1. Schematic of the rotary MOEMS switch: a) top view, b) serpentine spring, c) shape of the suspended platform and the circular-shaped springs, and d) zoomed view of the waveguides on the platform.

through a gap-closing mechanism involving electrodes and the serpentine spring, as previously mentioned.

The MOEMS structure features six electrodes: two V_{in1}, two V_{in2}, V_{GC}, and GND. Silicon dioxide (SiO_2) serves as the cladding material, while the core of the waveguides is made of SiN. The waveguide core has a width of 850 nm and a thickness of 435 nm, with a top and bottom cladding of 3.2 μm. An inverted taper is incorporated into each waveguide along the fixed portion and at the platform edge, with a minimum width of 400 nm and a length of approximately 20 μm, to enhance coupling efficiency across the gap (see Fig. 1(d), where each waveguide is numbered). The waveguides are spaced a minimum of 3.2 μm to prevent crosstalk between optical channels.

As seen in Fig. 1(c), the input waveguide initially aligns with the center waveguide (WG #4) in the absence of actuation voltages. Then, voltage V_{GC} is applied to reduce the gap, either in the initial state without rotation of the platform or after rotation in either the CW or the CCW direction, causing the platform to close by touching the two stoppers shown in Fig. 1(c).

2.2. MEMS structure description

The MEMS structure has a symmetrical design, consisting of comb fingers on both sides of a platform suspended by a serpentine spring. The entire structure is anchored through circular-shaped springs, which act as hinges during rotation. These circular springs have a width of 4 μm, and the structure has a thickness of 59 μm to meet fabrication requirements. To maintain symmetry during motion, there are 11 fixed fingers and 10 movable fingers on each side of the

Optics EXPRESS

structure. If the electrostatic force exceeds the stiffness of the movable part, the structure may deform [28]. To mitigate this risk, the design ensures the fingers are wide enough, selecting a width of 12 μm, with the outer free finger extending to a maximum length of 192 μm. These dimensions prevent excessive bending due to electrostatic forces, especially at large rotation angles. Figure 1(b) shows the serpentine spring attached to the suspended platform and free fingers. The serpentine spring is stiff enough so that the platform can rotate freely and align with the desired optical waveguide during operation. Moreover, it allows for the suspended platform to translate in order to close the gap. When no electrostatic force is applied to close the gap, the serpentine spring creates the restoring force that returns the suspended platform to its initial gap-open position. The lengths of the serpentine spring beam, which range from 90 μm to 205 μm, with a width of 4 μm, are carefully selected. Shorter beams would result in increased stiffness and require higher actuation voltages to close the gap, whereas longer beams would result in a very flexible serpentine spring, which would cause misalignment and out-of-plane motion.

The fixed fingers are connected to electrodes V_{in1} and V_{in2}, while the free comb fingers, anchored by the circular springs, are connected to ground (GND). Applying a voltage to V_{in1} induces CW rotation, while applying voltage to V_{in2} induces CCW rotation. As shown in Fig. 1(c), the suspended platform supports the optical waveguides. When a voltage is applied to the V_{GC} electrode, the gap between this electrode and the platform closes. The initial gap between the waveguides is 6 μm, which reduces to 2 μm upon actuation using the electrostatic gap-closing mechanism. During electrostatic actuation, the electrodes gradually approach each other until pull-in occurs, closing the gap. Stoppers, positioned on each side of the platform (Fig. 1(c)), prevent pull-in from causing a short circuit between the platform and V_{GC}. The pull-in voltage is expressed as:

$$V_{pi} = \sqrt{\frac{8}{27}\frac{kg^3}{\varepsilon A}} \tag{1}$$

where k is the stiffness, g is the gap between the electrode and the platform, ε is the permittivity, and A is the common area between the electrodes.

Angular misalignment of the rotary MOEMS switch can result in signal loss and degraded optical performance. This issue may arise if the platform undergoes translational motion instead of pure rotational motion. To mitigate this, a common center of rotation is ensured for the platform, as well as for all fixed and movable fingers.

Table 1 lists the physical dimensions of the MEMS structure.

Table 1. Dimensions of the rotary MOEMS switch

Component	Dimension (μm)
Finger width	12
Platform gap	6
Stopper gap	4
Serpentine spring length	90 – 205
Spring width	4
Circular-shaped spring radius	43

3. Simulations

Finite element method (FEM) simulations were conducted using the COMSOL Multiphysics software. The structural layer was assumed to be silicon with a (1 0 0) orientation and an elastic modulus (E) of 130 GPa [29]. As previously discussed, to induce rotation in the suspended platform, a voltage is applied to the V_{in1} or V_{in2} electrodes. Figure 2 shows the top view of the

Optics EXPRESS

deformed MEMS structure in both the CCW and CW states when an actuation voltage of 200 V is applied.

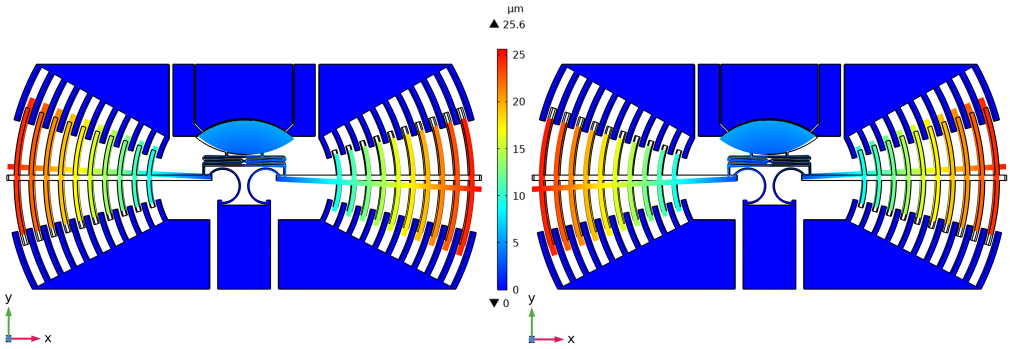

(a) (b)

Fig. 2. Rotation of the MOEMS structure for a 200 V actuation voltage: a) CW rotation using V_{in1}, b) CCW rotation using V_{in2}.

It is important to note that increasing the actuation voltage results in a higher angular displacement, peaking at 200 V before pull-in occurs at 207.5 V. The actuation voltage required to close the gap was determined using the same method, with 300 V needed to close the gap between the platform and the stoppers. The voltage levels observed in this work are consistent with electrostatic MEMS actuation principles, where forces scale quadratically with voltage. These high voltages (typically 50–200 V) are commonly required in MEMS devices [30–32], especially when microfabrication constraints lead to larger electrode gaps. To mitigate this, strategies such as reducing electrode gap distances or optimizing actuator stiffness can be considered. However, fabrication process limitations restrict gap minimization, and reducing stiffness may introduce unwanted out-of-plane motion, which could degrade optical performance. Moreover, the number of actuator combs could be increased at the cost of device area.

Figure 3(a) shows the simulation results for angular displacement vs actuation voltage (i.e., V_{in1} for CW rotation and V_{in2} for CCW rotation), reaching 2.3° at 200 V in both directions. Figure 3(b) shows the axial movement of the platform toward the electrode to close the air gap as a function of voltage (i.e., V_{GC}). The gap-closing motion is approximately 1.7 μm with an actuation voltage of 300 V. Additionally, gravity was applied to the platform to assess its effect on the suspended structure, showing a displacement of approximately 14 nm out-of-plane. Given that the thickness of the waveguide is 435 nm, this out-of-plane motion is not expected to have a significant impact on the optical insertion loss.

A 3D FDTD simulation was performed using the Ansys Lumerical software to estimate the insertion loss for both the open gap (6 μm) and closed gap (2 μm). The results showed that as the movable platform approached the stationary electrode with the fixed waveguides, the insertion loss decreased. Although the movable waveguide supports both polarizations, we focus on analyzing the TE polarization since we utilized TE grating couplers for testing. Initially, the insertion loss exceeded 2 × −7.7 dB. However, as depicted in Fig. 4(a), it decreased to 2 × −3.7 dB as the gap was reduced. Furthermore, the average back reflection was 9.45 % for each gap across the simulated wavelength range. The insertion loss does not reach zero due to a residual gap remaining after the gap closing process, as outlined in Section 2. This gap is not a consequence of the intended design but rather a limitation imposed by the fabrication grid size, which restricts the precise positioning of the stoppers relative to the fixed platform and,

Optics EXPRESS

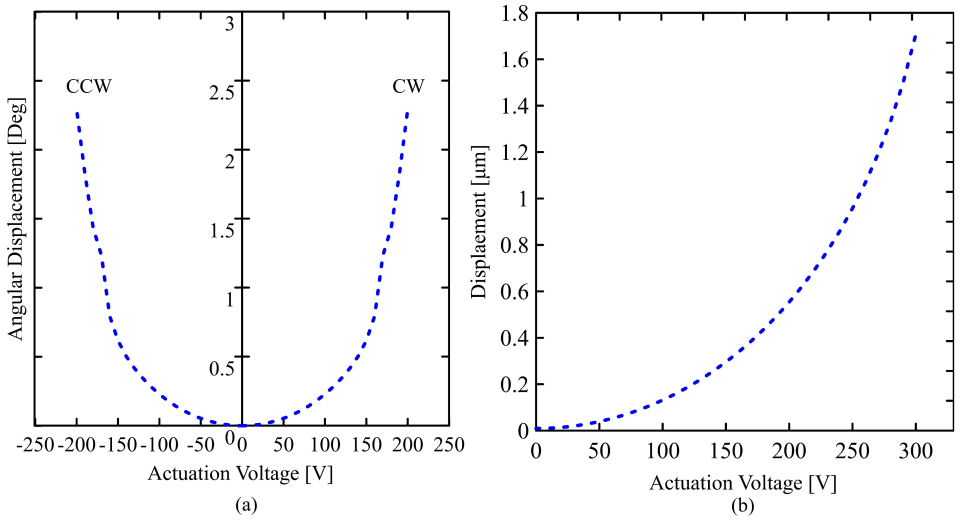

Fig. 3. Simulation results of the MOEMS structure: a) angular displacement versus V_{in1} (CW rotation) and V_{in2} (CCW rotation), b) gap closing displacement versus V_{GC}.

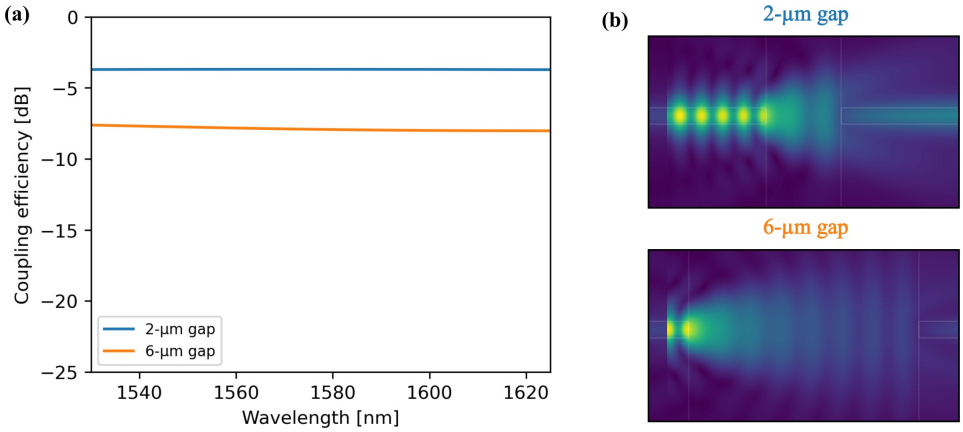

Fig. 4. Gap optical simulation results: a) coupling efficiency for the gap in closed and open states, and b) magnitude of the electric field for the gap in the closed and open states.

consequently, how closely the movable waveguides can align with the fixed waveguides after the gap is closed. The magnitude of the electric field for both the open and closed gaps is shown in Fig. 4(b).

The switching time for rotation and gap closing was evaluated through time-domain simulations with COMSOL Multiphysics. Rotating the platform to align the input channel from the initial state to WG #3 and #5 required 109 μs (see Fig. 1(d) for WG numbering). Switching to the first and last channels (i.e., WG #2 and #6) took 140 μs. Additionally, closing the gap to the stoppers required 53 μs. Since the middle channel (WG #4) relies solely on gap-closing actuation for efficient coupling, its switching time is also estimated to be 53 μs. For the remaining channels, including the gap-closing time, the switching time is determined to be 193 μs for WG #2 and

Optics EXPRESS

#6, and 162 μs for WG #3 and #5. Note that since WG #1 and #7 cannot be addressed with the platform rotation span, they are not considered here.

4. Fabrication

The rotary MOEMS switch was fabricated using a custom process developed by AEPONYX Inc. Figure 5 presents a cross-sectional view of the MOEMS switch. The process uses a SOI wafer with a device layer thickness of 59 μm and pre-etched cavities beneath it to facilitate the creation of the movable structure. The MEMS device is constructed of single-crystal silicon oriented along the (1 0 0) direction. This layer rests on a silicon oxide layer that serves to isolate the silicon device layer from the underlying silicon substrate, preventing electrical interaction. An additional silicon oxide layer is deposited on the top of the device layer as the bottom cladding of the optical waveguide. A SiN layer is deposited and patterned to form the waveguide cores. The next step in the fabrication process is the deposition of the top silicon oxide cladding. Metal pads are then deposited at predetermined areas to facilitate wire bonding to the printed circuit board (PCB). The presence of additional oxide on the structure, particularly on the suspended platform, could cause unwanted platform deformation and misalignment of the waveguides. To reduce residual stress, the top and bottom oxide cladding layers were etched away from areas other than the waveguides. The cross-section of the waveguides is 850 nm × 435 nm, while the top and bottom cladding layers are both 3.2 μm thick. Further fabrication details can be found in [25].

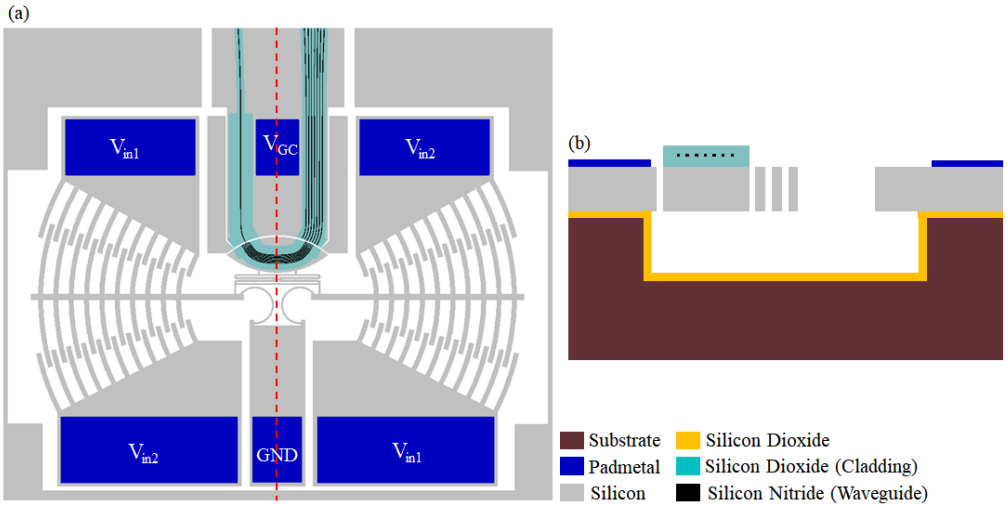

Fig. 5. Rotary MOEMS switch: a) top view,b) cross-sectional view.

Figure 6 shows the fabricated MOEMS switch, providing a visual confirmation that the fabricated device corresponds to the design schematic depicted in Fig. 1.

Optics EXPRESS

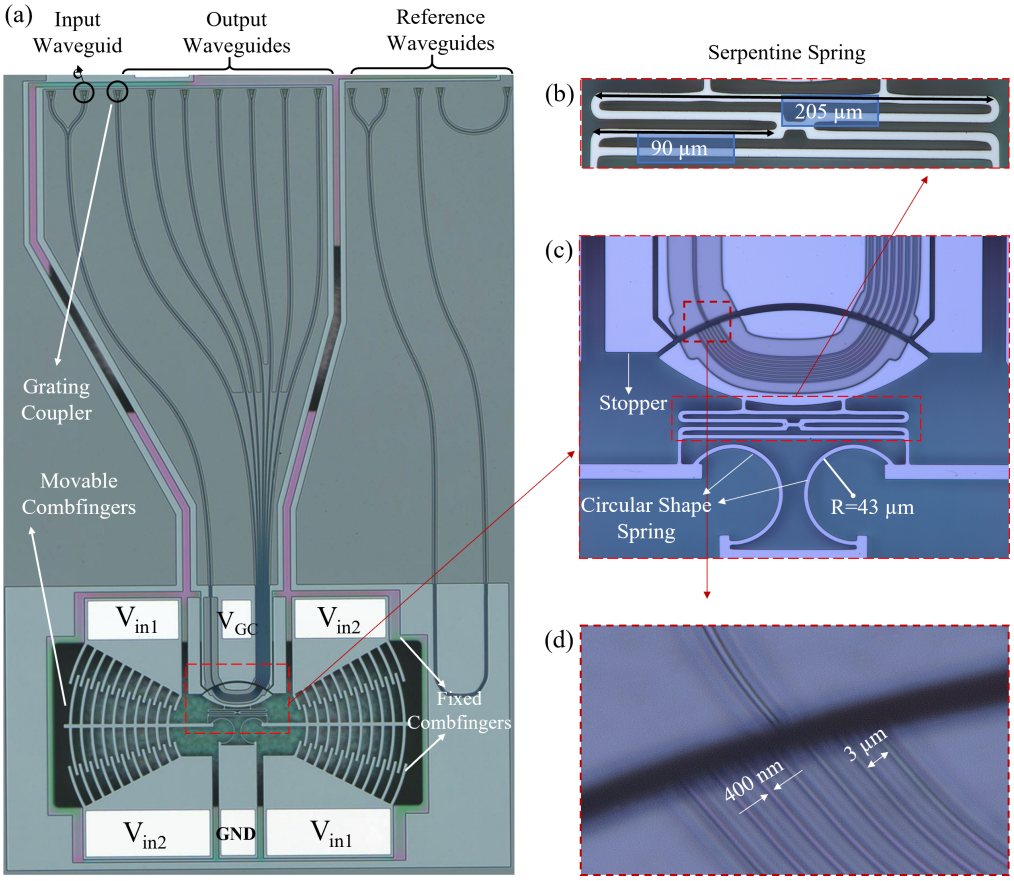

Fig. 6. Top view of the fabricated rotary MOEMS switch: a) entire structure, b) serpentine spring, c) suspended platform with waveguides and circular-shaped springs, d) magnified view of the waveguides.

5. Measurement results

Electromechanical measurements were conducted using a Keyence microscope (VHX7000) with a magnification of × 1000. The angular displacement and platform displacement required to close the gap are shown in Fig. 7(a) and Fig. 7(b), respectively. The rotary switch exhibits a rotational motion range of approximately 2.6° in the CCW direction and 2.9° in the CW direction. The actuation voltage required to achieve this angular displacement is 234 V, while the pull-in voltage is 235 V, slightly higher than the simulation results. This discrepancy is attributed to fabrication variations in the circular springs, which increased the stiffness of the structure, requiring more actuation voltage to achieve the same displacement.

In Fig. 7(a), the measured angular displacement results for both CW and CCW rotations are compared with simulations. The angular displacement of the platform could be measured under the optical microscope with a × 2500 magnification when the actuation voltage reached 60 V for CW rotation and 90 V for CCW rotation. While there is a slight discrepancy in CCW motion, the curves align well at 170 V, indicating approximately 1.5° of rotation. However, for CW motion, there is a more noticeable difference, with concordance observed around 155 V. Overall, the measurement results track reasonably well with the simulations.

Optics EXPRESS

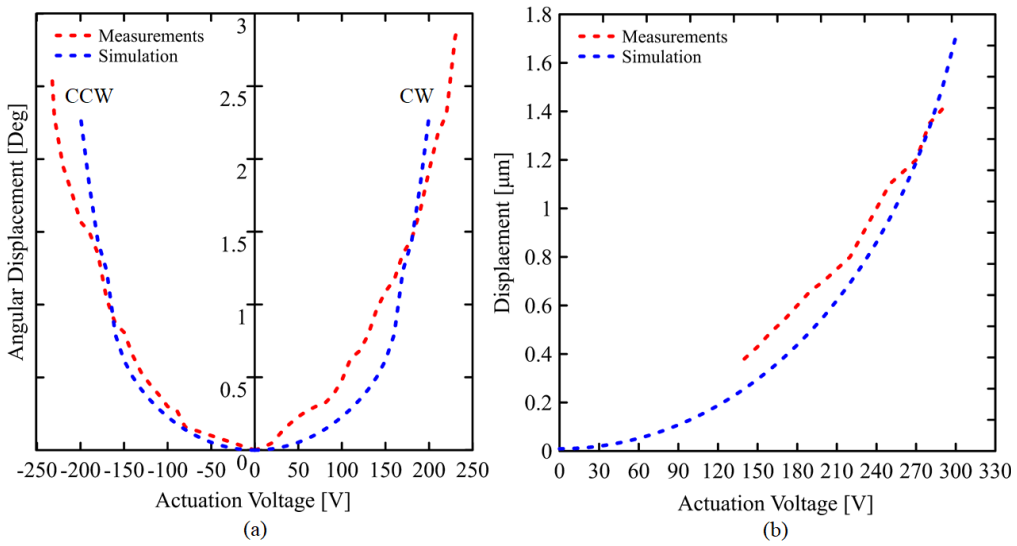

Fig. 7. Experimental and simulation results of the platform displacement: a) angular displacement, and b) gap closing displacement.

Figure 7(b) shows the simulation and measurement results for the gap-closing mechanism. Measurement of the gap-closing platform motion was not possible until 130 V was reached. The device required a slightly lower voltage than predicted by simulation to achieve the same platform displacement. While the simulation indicated that 300 V would be needed to close the 6 μm gap between the platform and the electrode, a slightly lower voltage of 290 V was required experimentally. It could be explained because the average measured gap open was 5.6 μm due to the fabrication discrepancy.

Optical transmission measurements were conducted using the test setup outlined in [26]. A baseline was established by measuring the coupling efficiency with the gap open, and it was compared with measurements obtained with the gap closed for each channel. In the initial state of the rotary MOEMS switch, the input waveguide is aligned with the central waveguide (WG #4) on the platform, and only an actuation voltage to close the gap was applied. For the other waveguides, specific voltages were applied to each electrode pair to rotate the platform in both CCW and CW directions, aligning the input with each output. The gap was then closed.

The electrostatic force behaves non-linearly, making a pull-in event inevitable when large rotations are achieved. When the actuation voltage is applied to rotate the platform, either CW or CCW, controlling the deformation becomes more challenging as the voltage approaches the pull-in voltage. This results in unpredictable movements and variations in gap size due to the proximity of the platform to the gap-closing electrode. Consequently, when the gap-closing electrode is engaged, these variations can cause premature pull-in, especially for the outermost waveguides (i.e., WG #1 and WG #7). This instability led the platform to collapse unpredictably into different regions of the electrodes rather than aligning correctly beyond the previously reported angular range, i.e., 2.9° in the CW direction for WG #1 and 2.6° in the CCW direction for WG #7. As a result, only five out of the seven waveguides could be properly aligned to the input waveguide with an actuation voltage of 234 V. The scalability of the optical switch, specifically its ability to align to a larger number of waveguides (e.g., 7), can be achieved through the tuning and optimization of the MEMS structure. The rotational capability of the platform can be enhanced by modifying the circular-shaped springs to reduce their stiffness. This can be achieved by adjusting the spring dimensions, such as increasing the radius of the circular-shaped spring, while

Optics EXPRESS

ensuring that such modifications do not introduce unwanted out-of-plane or translational motion. Additionally, the comb-drive actuation mechanism can be optimized by increasing the number of comb fingers or enhancing the overlap between fixed and movable fingers to generate a greater electrostatic torque. These improvements, focused on maximizing angular displacement and actuation efficiency, would allow the MEMS platform to align with more output waveguides, thereby enhancing the scalability of the optical switch. Figure 8 illustrates the alignment of the five waveguides with the input waveguide under the gap-closing condition.

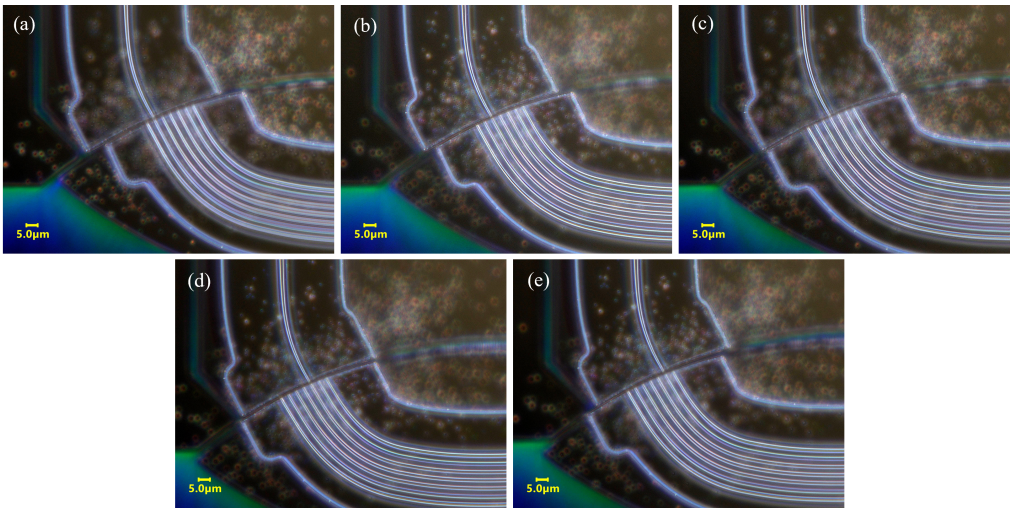

Fig. 8. Microscope image of each waveguide alignment on the platform with the input waveguide: a) WG %2, b) WG %3, c) WG %4, d) WG %5, and e) WG %6.

To normalize the losses for each channel, a reference waveguide was fabricated with the same length as WG #1, as depicted in Fig. 1(a). This reference exhibited losses of approximately −27.69 dB due to the two grating couplers. Table 2 lists the results after normalizing the coupling efficiency by the insertion loss of the grating couplers. The values presented are the average coupling efficiency for each waveguide over the wavelength range of 1540 nm to 1625 nm, covering the C and L bands for telecommunications applications. Due to the limitations of the grating couplers used in the design, the wavelength range was set to start from 1540 nm. As shown in the table, the coupling efficiency improved significantly with the gap-closing mechanism activated. Notably, the average closed gap was measured at 1.08μm, which likely enhances the switch's efficiency.

Table 2. Coupling efficiency of each output waveguide

Waveguide	Gap open [dB]	Gap closed [dB]
#2	−13.25	−6.49
#3	−14.29	−4.95
#4	−12.09	−4.08
#5	−14.16	−5.01
#6	−13.00	−6.64

Figure 9 presents the coupling efficiency from 1540 nm to 1625 nm for each of the five output waveguides, both with the gap open (GO) and closed (GC). The average coupling efficiency for all five channels when the gap is closed is −5.57 dB, showcasing a power difference between

Optics EXPRESS

channels of less than 2 dB, thus outperforming the MOEMS presented in [23]. Notably, as previously mentioned, the gap in both the open and closed states was smaller than the expected value due to fabrication variations. This discrepancy resulted in a higher coupling efficiency for the switch in both conditions compared to simulations. Furthermore, the gap-closing mechanism improved the efficiency by an average of 8.03 dB.

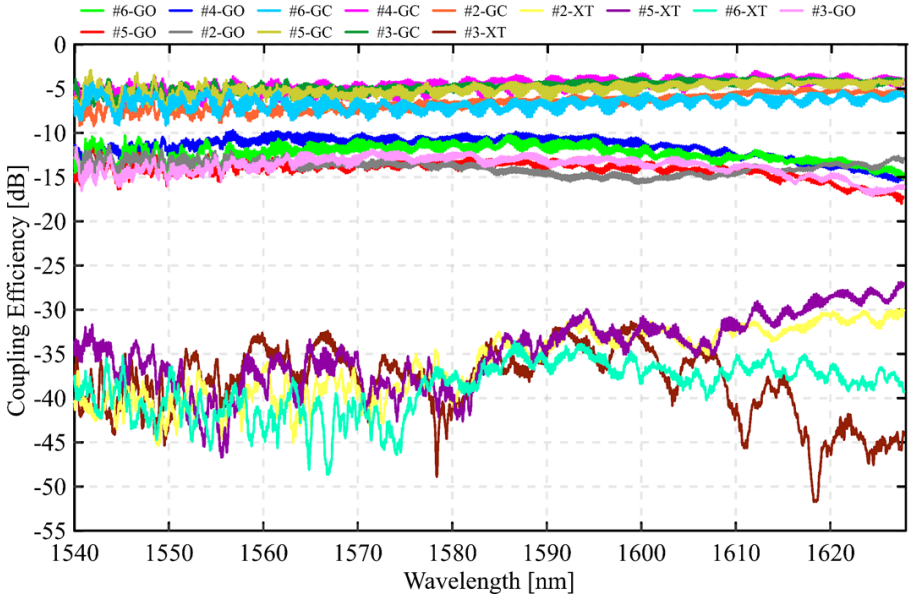

Fig. 9. Measured coupling efficiency of the waveguides when the gap is open and closed, where GO is Gap Open, GC is Gap Closed, and XT represents crosstalk.

The undesirable leakage of the light from a channel to adjacent waveguides, known as crosstalk, was measured and is presented in Fig. 9. To perform this measurement, three detectors were used simultaneously. For instance, when the input signal was routed through WG#4, the adjacent waveguides on its right and on its left (WG#3 and WG#5, respectively) were also connected to detectors. This configuration allowed the measurement of any leakage into the adjacent waveguides. This allowed to accurately record the crosstalk into the adjacent channels after closing the gap.

The plot shows that crosstalk values fluctuate around −35 dB over the wavelength range of 1540 nm to 1625 nm. This level of crosstalk demonstrates effective isolation between the channels, ensuring signal integrity with minimal interference.

6. Discussion

Previous studies on electrothermal and electrostatic actuation mechanisms for MOEMS switches highlight distinct advantages and limitations. For instance, work in [26] demonstrated that electrothermal actuation requires higher power consumption (i.e., 219 mW for 6 μm displacement) compared to the electrostatic actuation proposed here, which operates with near-zero power consumption to achieve 2.9° of rotation, equivalent to an arc length of 8.5 μm.

The operational wavelength range of the proposed MOEMS switch is broader compared to other optical switches, such as those employing MMI and MZI structures. For example, the MZI switch proposed in [33] operates within a limited wavelength range of 1540 nm to 1565 nm, whereas the proposed switch operates from 1540 nm to 1625 nm. In terms of crosstalk, MOEMS switches such as ours exhibit lower crosstalk compared to other technologies. The

Optics EXPRESS

MOEMS switch in this work exhibits crosstalk of around −35 dB, which is better than the crosstalk performance of MMI and MZI switches. For instance, the crosstalk for the MZI switches presented in [22,34] is −10 dB. Another important class of switches is all-to-all switches, which include the N × N switch. For instance, Seok *et al.* [35] presented a 64 × 64 switch using a matrix architecture, these switches provide complete inter-connectivity with a low insertion loss of 3.7 dB, and fast switching times of 0.91 μs. However, this device is based on a vertical adiabatic coupler design in which the fabrication process is more complex and multilayered. Furthermore, with this approach the waveguides cannot by cladded, which can create packaging challenges.

In this work, it is possible to cover 25 output channels with a two-level hierarchical structure. Moreover, if we can use all the output waveguides to have a 1 × 7 switch, it would scale to 49 output channels within the same architecture. Additionally, we could use the actuator structure presented here and replace the channel waveguides on the platform by a planar waveguide with a curved mirror at its edge to increase the number of addressable channels of a single switch to more than 7, as presented by [27]. This shows potential approaches to create a scalable switch fabric but it is worth noting that it would come at the cost of increased insertion loss if a multilevel architecture was employed or higher mechanical stress on the platform if the planar waveguide design is used.

Additionally, SiN has been utilized in various MOEMS switches, such as the 1 × 5 switch in [24]. That switch has a maximum insertion loss of 7.5 dB and a minimum insertion loss of 2.2 dB, operating within the same wavelength range of 1540 nm to 1625 nm, demonstrating the broadband capabilities of SiN waveguides. However, the 1 × 5 switch exhibits a 5.3 dB variation between the minimum and maximum insertion loss. In contrast, the variation in the proposed 1 × 5 switch is only 1.86 dB, demonstrating more consistent power loss across all channels, a notable performance improvement.

Compared to optical waveguides made of silicon (Si) [36], SiN waveguides used in this work offer several advantages, including lower overall losses at near-infrared (NIR) wavelengths and more consistent performance due to smaller refractive index contrast. SiN waveguides exhibit lower propagation insertion loss than silicon waveguides due to reduced sidewall scattering losses. Additionally, SiN can be used across a wide wavelength range due to its large transparency window [36,37].

Nevertheless, SiN waveguides and suspended platforms present challenges related to mechanical stability and optical performance that must be addressed. For instance, the suspended SiN structures reported by Grottke et al. [38] can deform and exhibit stress-induced misalignment after fabrication, leading to increased insertion losses. To mitigate this, the SiN layer thickness and etching process require optimization to enhance mechanical robustness and reduce residual stresses.

Another critical aspect is the precise integration of movable components while minimizing scattering losses at the edges of suspended regions. As demonstrated by Seok et al. [39], achieving low stitching losses and maintaining low-loss optical propagation over suspended sections in large-scale designs demand extremely tight fabrication tolerances.

Table 3 provides a comparison of various published switches employing SiN waveguides. The MOEMS switch in this work operates with electrostatic actuation, offering a wavelength range of 1540 nm to 1625 nm, near-zero power consumption, a switching time of 162 μs, and an insertion loss of 6.5 dB. Compared to other devices, it matches the zero power consumption of similar electrostatic switches but demonstrates slightly higher insertion loss and longer switching times. In contrast, thermo-optic switches, while faster (down to 4.7 μs) and sometimes exhibiting lower insertion loss, consume significantly more power (up to 290 mW). Additionally, electrothermal actuation, as seen in some MEMS devices, can result in high power consumption (189-219 mW).

Optics EXPRESS

Table 3. Comparison of various switching mechanisms employing silicon nitride as the waveguide material.

Reference	Switch Type	Switching Mechanism	Wavelength Range [nm]	Power Consumption [mW]	Switching Time	Insertion Loss [dB]	Array Size	Loss per Port [dB/port]	Crosstalk [dB]	Area per Port [μm^2/port]
[26]	MEMS	Electrothermal Actuation	1550-1620	189-219	3 ms	1.6±0.06	1×1	1.6	−40	875,000
[40]	MEMS	Electrostatic Actuation	1540-1620	zero	N/A	2.2–5.39	1×5	0.44–1.5	−30	175,000
[23]	MEMS	Electrostatic Actuation	1500-1630	zero	150 μs	7.89	1×3	1.55–1.94	−30	28,167
[33]	MMI-MZI	Thermo-Optic	1540-1565	1.07	4.7 μs	0.5	2×2	0.25	−30	3,375
[22]	MZI	Electro-Optic	N/A	N/A	57.78 ns	N/A	1×2	N/A	N/A	2,286
[34]	MZI	Thermo-Optic	1554.7	290	10 ms	2.4±0.4	3×3–4×4	0.11–0.15	−10	197,000
[41]	MZI	Thermo-Optic	1530-1610	5.9	840 μs	11.7	1×2	5.85–7.1	−20.5 to −19.6	1,800,000
[42]	Meta-Surface	Voltage	630	90	100 ms	1	1×2	0.5	−11.24	9.63
[35]	MEMS	Electrostatic Actuation	1460-1580	near zero	0.91 μs	3.7	64×64	0.058	N/A	12,000
[39]	MEMS	Electrostatic Actuation	1540-1625	zero	< 400 ns	9.8	240×240	0.04	−70	66,667
This Work	MEMS	Electrostatic Actuation	1540-1625	zero	162 μs	6.5	1×5	1.11	−35	175,000

7. Conclusion

This work introduced a novel electrically actuated 1 × 5 SiN integrated rotary MOEMS switch capable of achieving significant rotational angles, with 2.9° in the CW direction and 2.6° in the CCW direction, covering 5 channels with an actuation voltage of 234 V. The rotary MOEMS switch demonstrated consistent power loss across the 5 channels, with an average insertion loss of −5.57 dB. Furthermore, due to the SiN-based waveguides, the switch has the potential to operate over a broader spectrum. In this work, it was successfully tested within the wavelength range of 1540 nm to 1625 nm. The use of the electrostatic actuation mechanism with near-zero power consumption makes the proposed 1 × 5 rotary MOEMS switch a promising candidate for applications in data centers.

By employing circular-shaped springs designed to minimize axial movement at the pivot point, the suspended platform was effectively controlled, allowing for precise alignment of the input and output waveguides. As a result, the difference between the maximum and minimum insertion loss was limited to 1.86 dB, ensuring uniform losses across all channels—a critical performance metric for data center applications.

The experimental results revealed some discrepancies between simulation and measurement, primarily due to fabrication variations affecting the springs and consequently altering the mechanical behavior. These discrepancies led to increased stiffness and higher actuation voltage requirements to achieve the same angular displacements. Despite these challenges, the switch successfully covered 5 out of the 7 available waveguides on the platform and demonstrated strong overall performance.

Future iterations of the switch aim to incorporate a latch mechanism to prevent undesired motion at higher actuation voltages. Additionally, further enhancements will focus on improving device performance, reducing power consumption further, enhancing coupling efficiency, and broadening the switch applicability in optical communication networks.

Funding. AEPONYX ((CRDPJ 530551 - 18); PRIMA Quebec ((R16-46-002 PSO); Natural Sciences and Engineering Research Council of Canada (CRDPJ 530551 - 18).

Acknowledgement. The authors would like to thank AEPONYX Inc. for access to their test facilities, device fabrication, and technical support.

Disclosures. AASR: AEPONYX (F,P), SS: AEPONYX (F,P), JP: AEPONYX (F), MM: AEPONYX (F,P), FN: AEPONYX (F,P)

Data availability. Data is available upon reasonable request.

Optics EXPRESS

References

1. A. Ghiasi, "Large data centers interconnect bottlenecks," Opt. Express **23**(3), 2085 (2015).
2. Y. Shi, Y. Zhang, and Y. Wan, "Silicon photonics for high-capacity data communications," Photonics Res. **10**(9), A106 (2022).
3. N. Margalit, C. Xiang, and S. M. Bowers, "Perspective on the future of silicon photonics and electronics," Appl. Phys. Lett. **118**(22), 220501 (2021).
4. X. Tu, C. Song, and T. Huang, "State of the Art and Perspectives on Silicon Photonic Switches," Micromachines **10**(1), 51 (2019).
5. S. Bernabé, Q. Wilmart, and K. Hasharoni, "Silicon photonics for terabit/s communication in data centers and exascale computers," Solid-State Electron. **179**, 107928 (2021).
6. Y. Zhao, X. Xue, X. Ren, *et al.*, "Optical Switching Data Center Networks: Understanding Techniques and Challenges," Computer Networks and Communications (2023).
7. Q. Cheng, Y. Huang, H. Yang, *et al.*, "Silicon Photonic Switch Topologies and Routing Strategies for Disaggregated Data Centers," IEEE J. Sel. Top. Quantum Electron. **26**(2), 1–10 (2020).
8. M. Nance Hall, K.-T. Foerster, and S. Schmid, "A Survey of Reconfigurable Optical Networks," Opt. Switch. Netw. **41**, 100621 (2021).
9. C. Li, D. Liu, and D. Dai, "Multimode silicon photonics," Nanophotonics **8**(2), 227–247 (2019).
10. Y. Shang, J. Zhou, and H. Jiang, "Optimal design of a 4×4 MMI thermal optical switch with trapezoidal air trenches," Appl. Opt. **62**(6), 1521 (2023).
11. S. Sun, Y. Che, and Y. Xie, "Multimode optical switch based on cascaded Mach–Zehnder interferometer waveguides," Opt. Lett. **48**(20), 5336 (2023).
12. T. Kita and M. Mendez-Astudillo, "Ultrafast Silicon MZI Optical Switch With Periodic Electrodes and Integrated Heat Sink," J. Lightwave Technol. **39**(15), 5054–5060 (2021).
13. M. Mendez-Astudillo, M. Okamoto, and Y. Ito, "Compact thermo-optic MZI switch in silicon-on-insulator using direct carrier injection," Opt. Express **27**(2), 899 (2019).
14. X. Chen, J. Lin, and K. Wang, "A Review of Silicon-Based Integrated Optical Switches," Laser Photonics Rev. **17**(4), 2200571 (2023).
15. H. Sattari, A. Toros, T. Graziosi, *et al.*, "Bistable silicon photonic MEMS switches," in *MOEMS and Miniaturized Systems XVIII*, W. Piyawattanametha, Y.-H. Park, and H. Zappe, eds. (SPIE, San Francisco, United States, 2019), p. 13.
16. N. Quack, A. Y. Takabayashi, and H. Sattari, "Integrated silicon photonic MEMS," Microsyst. Nanoeng. **9**(1), 27 (2023).
17. S. Sharma, S. Nabavi, and A. A. S. Rabih, "Hybrid MEMS Actuator With 3 Degrees-of- Freedom for Efficient Planar Optical Switching," J. Microelectromech. Syst. **32**(6), 593–603 (2023).
18. X. Ma and G.-S. Kuo, "Optical switching technology comparison: optical mems vs. other technologies," IEEE Commun. Mag. **41**(11), 50–57 (2003).
19. T. Barwicz and H. Haus, "Three-dimensional analysis of scattering losses due to sidewall roughness in microphotonic waveguides," J. Lightwave Technol. **23**(9), 2719–2732 (2005).
20. D. S. Kim, S. G. Yoon, and G. E. Jang, "Refractive index properties of SiN thin films and fabrication of SiN optical waveguide," J. Electroceram. **17**(2-4), 315–318 (2006).
21. A. Senichev, S. Peana, and Z. O. Martin, "Silicon nitride waveguides with intrinsic single-photon emitters for integrated quantum photonics," ACS Photonics **9**(10), 3357–3365 (2022).
22. L. Dong, K. Zhao, K. Chen, *et al.*, "Hybrid Si3N4/electro-optic polymer waveguide Mach-Zehnder interferometer for high-speed electro-optic switching," in *Thirteenth International Conference on Information Optics and Photonics (CIOP 2022)*, Y. Yang, ed. (SPIE, Xi'an, China, 2022), p. 260.
23. S. Sharma, N. Kohli, and J. Brière, "Integrated 1×3 MEMS silicon nitride photonics switch," Opt. Express **30**(12), 22200 (2022).
24. S. Sharma, N. Kohli, and M. Ménard, "An Integrated 1 by 5 MEMS Silicon Nitride Photonics Switch," J. Lightwave Technol. **42**(13), 4585–4597 (2024).
25. B. Barazani, A. Gascon, and C. Coia, "Broadband 1 x 4 Silicon Nitride Photonic Switch Fabricated on a Hybrid Electrothermal and Electrostatic MEMS Platform," J. Lightwave Technol. **41**(21), 6710–6722 (2023).
26. A. A. S. Rabih, S. Sharma, and J. Pita, "Two-axis MEMS positioner for waveguide alignment in silicon nitride photonic integrated circuits," Opt. Express **31**(19), 30797 (2023).
27. J. Briere, M. Elsayed, and M. Saidani, "Rotating Circular Micro-Platform with Integrated Waveguides and Latching Arm for Reconfigurable Integrated Optics," Micromachines **8**(12), 354 (2017).
28. W.-M. Zhang, H. Yan, and Z.-K. Peng, "Electrostatic pull-in instability in MEMS/NEMS: A review," Sens. Actuators, A **214**, 187–218 (2014).
29. M. A. Hopcroft, W. D. Nix, and T. W. Kenny, "What is the Young's Modulus of Silicon?" J. Microelectromech. Syst. **19**(2), 229–238 (2010).
30. A. C. Atik, M. D. Özkan, and E. Özgür, "Modeling and fabrication of electrostatically actuated diaphragms for on-chip valving of MEMS-compatible microfluidic systems," J. Micromech. Microeng. **30**(11), 115001 (2020).
31. H. M. Ouakad and F. Najar, "Nonlinear Dynamics of MEMS Arches Assuming Out-of-Plane Actuation Arrangement," J. Vib. Acoust. **141**(4), 041010 (2019).

Optics EXPRESS

32. E. W. Schaler, T. I. Zohdi, and R. S. Fearing, "Thin-film repulsive-force electrostatic actuators," Sens. Actuators, A **270**, 252–261 (2018).
33. F. Duan, K. Chen, and D. Chen, "Low-power and high-speed 2 × 2 thermo-optic MMI-MZI switch with suspended phase arms and heater-on-slab structure," Opt. Lett. **46**(2), 234 (2021).
34. S. Kovaios, A. Tsakyridis, and G. Giamougiannis, "Generalized Mach Zehnder Interferometers Integrated on Si_3 N_4 Waveguide Platform," IEEE J. Sel. Top. Quantum Electron. **29**(6: Photonic Signal Processing), 1–9 (2023).
35. T. J. Seok, N. Quack, and S. Han, "Large-scale broadband digital silicon photonic switches with vertical adiabatic couplers," Optica **3**(1), 64 (2016).
36. J. Wang and Y. Long, "On-chip silicon photonic signaling and processing: a review," Sci. Bull. **63**(19), 1267–1310 (2018).
37. C. Xiang, W. Jin, and J. E. Bowers, "Silicon nitride passive and active photonic integrated circuits: trends and prospects," Photonics Res. **10**(6), A82 (2022).
38. T. Grottke, W. Hartmann, and C. Schuck, "Optoelectromechanical phase shifter with low insertion loss and a 13pi tuning range," Opt. Express **29**(4), 5525 (2021).
39. T. J. Seok, K. Kwon, and J. Henriksson, "Wafer-scale silicon photonic switches beyond die size limit," Optica **6**(4), 490 (2019).
40. S. Sharma, N. Kohli, M. Ménard, *et al.*, "1× 5 silicon nitride mems optical switch," in *2022 European Conference on Optical Communication (ECOC)*, (IEEE, 2022), pp. 1–4.
41. S. Sun, X. Sun, and T. Lian, "1 × 2 mode-independent polymeric thermo-optic switch based on a Mach–Zehnder interferometer with a multimode interferometer," Opt. Express **31**(8), 12049 (2023).
42. A. Alquliah, M. Elkabbash, and J. Cheng, "Reconfigurable metasurface-based 1 × 2 waveguide switch," Photonics Res. **9**(10), 2104 (2021).